

Orbital Reconstruction in a Self-assembled Oxygen Vacancy Nanostructure

H. Jang¹, G. Kerr¹, J. S. Lim², C.-H. Yang², C.-C. Kao³, and J.-S. Lee^{1,*}

¹Stanford Synchrotron Radiation Lightsource, SLAC National Accelerator Laboratory, Menlo Park, California 94025, USA

²Department of Physics, KAIST, Yuseong-gu, Daejeon 305-701, South Korea

³SLAC National Accelerator Laboratory, Menlo Park, California 94025, USA

*jslee@slac.stanford.edu

ABSTRACT

We demonstrate the microscopic role of oxygen vacancies spatially confined within nanometer inter-spacing (about 1 nm) in BiFeO₃, using resonant soft X-ray scattering techniques and soft X-ray spectroscopy measurements. Such vacancy confinements and total number of vacancy are controlled by substitution of Ca²⁺ for Bi³⁺ cation. We found that by increasing the substitution, the in-plane orbital bands of Fe³⁺ cations are reconstructed without any redox reaction. It leads to a reduction of the hopping between Fe atoms, forming a localized valence band, in particular Fe 3*d*-electronic structure, around the Fermi level. This band localization causes to decrease the conductivity of the doped BiFeO₃ system.

Introduction

In an intrinsic manner, oxygen vacancies always reside in all oxide compounds modulating chemical and physical properties on the scheme of defect chemistry. Beyond regarding this as an intrinsic defect, nowadays the oxygen vacancy has been considered as a parameter for controlling functionalities of oxide compounds such as quantum materials with strong electron correlation¹⁻⁵ and energy materials⁶⁻⁹. In this context, it has been demonstrated that changes in electronic conductivity on the correlated perovskite ABO_3 ^{3,4} and Li-based batteries^{6,8} are associated with total oxygen vacancies. Furthermore, the spatially inhomogeneous distribution of the oxygen vacancies is regarded as another important parameter, as demonstrated in multiferroic $BiFeO_3$ ¹⁰⁻¹⁴. Ferroelectric polarization in $BiFeO_3$ can be tuned by an external electric field. Meanwhile, the external electric field additionally induces oxygen vacancy migration because oxygen vacancies are positively charged^{11,15}, leading to a switchable photovoltaic effect in $BiFeO_3$ ^{10-14,16}. In spite of the vacancy's importance in those applications, however, a role of oxygen vacancies has been puzzling and discussed only conceptually. Thus, the lack of microscopic understanding limits the improvement of the functionalities of oxide compounds.

For this reason, we discuss the microscopic role of oxygen vacancies for a representative multiferroic photovoltaic system, $BiFeO_3$. In general, the photovoltaic effect is associated with a modification of the electrons present in both the valence and conduction band when a material absorbs energy via the light¹⁷. However, the multiferroic $BiFeO_3$ case is more complicated because the oxygen vacancy's migration is also affected by the built-in

electric field. Here, we investigate an electronic structure with varying the oxygen vacancy in BiFeO₃ using resonant soft X-ray scattering and soft X-ray absorption spectroscopy measurement and corresponding atomic model calculations. Considering previous works, the number of the oxygen vacancies in BiFeO₃ can be readily controlled with Ca²⁺ substitution (x) for Bi³⁺ cations – Bi_{1-x}Ca_xFeO_{3- δ} (hereafter, BCFO)^{15,18}. Each planar defect an arrangement of Bi/Ca cations is adopted and promotes the formation of oxygen vacancy, showing a brownmillerite-like intra-plane, which leads to a superstructure (see Fig. 1a)^{15,19}. Considering the previous TEM studies¹⁹⁻²¹, furthermore, the oxygen vacancy in the superstructure is confined within a single unit cell in a self-assembled manner and the planar structures periodically appear at a few nanometers interval depending on the Ca substitution ratio (see Methods).

In the doped BCFO case, anionic electron number is reduced by the formation of positively charged oxygen-vacancy¹⁵. In this manner, electron-hole pairs are modified by the oxygen vacancy. According to the reported photovoltaic properties of BCFO as a function of the vacancy concentration²², however, it does not show a monotonic increase even in a monotonic enhancement of the oxygen vacancy in BCFO. In particular, such effect decreases beyond $x \sim 15\%$ ²². This means that the reported diode effect^{10, 11} of BiFeO₃ cannot be simply employed for explaining a change in BCFO via the oxygen vacancy. This implies that near cations (i.e., Fe in this case) chemically responds to the oxygen vacancies, leading to our attention for a role of oxygen vacancies via spectroscopic scheme such as electronic configuration.

Results

Figure 2a shows O *K*-edge X-ray absorption spectroscopy (XAS) spectra on Ca²⁺ 25% doped BCFO sample (BCFO25), aiming to address the spectroscopy scheme of the oxygen vacancy. The spectra were acquired by recording the total electron yield (TEY) – details of the experimental geometry are shown in Fig. 2b (see Methods). The spectral features represent hybridization effects between O *2p*-Fe *3d* bands²³. There are two pronounced features around $E = 527.4$ eV and 528.8 eV, corresponding to the Fe *t*_{2g} and *e*_g orbitals coupled with oxygen bands, respectively. Interestingly, these features are nearly identical to un-doped BiFeO₃ (green lines in Fig. 2a), although the number of vacancies in the two samples is completely different. Moreover, the polarization dependence ($E//a$ and $E//c$), which is sensitive to orbital anisotropy²⁴ and crystal symmetry²⁵, is similar to BiFeO₃. This means that even with substantial oxygen vacancies, a change in the electronic structure of oxygen is hard to observe by this XAS measurement.

For the next step, we employed the site-selective spectroscopic technique – resonant soft X-ray scattering (RSXS). Since the oxygen vacancies in Ca²⁺ doped BiFeO₃ are confined periodically¹⁵, this allows the exploration of electronic configurations around an oxygen vacancy. Figure 2c shows a θ - 2θ scan of BCFO25 at $E \sim 525$ eV – details of the experimental geometry are shown in Fig. 2b. It clearly shows the superstructure reflection, $\mathbf{q} = (001)$, indicating periodically confined vacancies, which is consistent with the structural formation as shown in Fig. 1a. To investigate the site-selective (i.e., confined vacancies) spectroscopic features, energy scans at fixed \mathbf{q} were performed with

two (σ and π) incident polarizations (Fig. 2d). Note that electronic anisotropy can be resolved by controlling σ or π polarization in this RSXS measurement^{26,27}. The measured RSXS profiles are quite unlike XAS spectra, showing the polarization dependence around the anisotropic Fe t_{2g} and e_g orbital bands hybridized with oxygen. In this context, the difference in the RSXS intensity profile between σ and π represents the anisotropic Fe 3d orbital state as modified by the oxygen vacancies.

Since Fe cations in BCFO are chemically correlated with the oxygen vacancies, we need to scrutinize the Fe electronic structures. Figure 3a shows the XAS spectrum for the Fe $L_{2,3}$ -edges. The spectral features are almost identical to the known Fe³⁺ cation feature^{23,28}. This means that the Fe valence is retained as a single 3+ state. This is in agreement with atomic multiplet calculations²⁹ on the single valence state under D_{4h} symmetry (see Methods). Moreover, this calculation can generate linear dichroism ($LD = E//a - E//c$). The calculated LD is comparable to experimental results (Fig. 3b) except for a small deviation around the in-plane orbital characters (xy and x^2-y^2). This deviation, in particular the x^2-y^2 character, is more pronounced in more heavily doped system (30% doped BCFO30). These findings might be associated with the implication (i.e., Fe 3d orbital state modified by oxygen vacancy) of O K -edge RSXS measurements. In other words, the in-plane orbital characters as modified by the oxygen vacancies undergo an additional anisotropic effect beyond the tetragonal crystal symmetry.

We now consider RSXS measurements at the Fe $L_{2,3}$ -edges, for exploring Fe orbital anisotropy around the oxygen vacancies. Like the observed superstructure at the O K -edge, we clearly see a superstructure reflection at $\mathbf{q} = (001)$, in addition to the second

order (002) reflection (Fig. 4a inset). In the Fe *L*-edge RSXS study, we focused on the $q = (002)$ peak of BCFO25. Figure 4a shows the Fe *L*-edge RSXS profile for σ incident polarization. Note that the Fe profiles have been subtracted by a diffuse scattering part, e.g. fluorescence background (see Supplementary Information). In comparison with the Fe XAS spectrum, the RSXS profile is quite complicated. This complexity arises from modification of the Fe local structure by the oxygen vacancies. The elongated octahedral Fe (D_{4v}) coordination in doped BiFeO₃ can be transformed to tetrahedral (T_d) and square pyramidal (C_{4v}) symmetry via oxygen vacancies^{19,30}. The resonant scattering is produced by the scattering form factor which is basically determined from the crystal symmetry. Therefore, the Fe RSXS profile in Fig. 4a is constructed by all symmetries in the BCFO. Accordingly, the current RSXS profile corresponding to both the complicated structural effects and regarding their Fe spectroscopic information causes a difficulty in exploring the Fe 3*d* orbital state modified by the oxygen vacancy.

To overcome this difficulty, we employed polarized X-rays and the principle of Brewster's angle³¹ in this measurement. Moreover, this is why we focused on the (002) peak of BCFO25 (see Supplementary Information). Note that we do not control a polarization of the out-going photon, indicating the scattered X-ray always shows both σ_f and π_f polarizations. Considering the principle, in here $\theta_i + \theta_f \sim 90^\circ$ Brewster geometry, structural contribution (via $\pi_i - \pi_f$ channel) is drastically suppressed in incident π_i -polarization, while the structural contribution (via $\sigma_i - \sigma_f$ channel) is still large in incident σ_i -polarization³². As a consequence, we clearly observed the Fe spectroscopic behavior via the $\pi_i - \sigma_f$ channel of incident π_i -polarization at $q = (002)$ (shown in Fig. 4b). Remarkably, there are only two pronounced features around $E = 706$ eV and 708 eV,

agreeing with the implication of the Fe *L*-edge XAS measurements, which respectively corresponds to xy in t_{2g} orbital bands and x^2-y^2 in e_g orbital ones. This indicates that the Fe^{3+} band, in particular in-plane orbital bands, becomes anisotropic around the Fermi level, revealing the role of oxygen vacancy in BCFO system.

Discussion

Considering the Fe octahedral structure in the BCFO, the in-plane orbital characters in the crystal symmetry of the BCFO is not energetically preferred because of the *c*-axis elongation, showing the self-assembled structure as shown in Fig. 1a. Nevertheless, local in-plane Fe orbital bands on the self-assembled layers formed by the oxygen vacancy are clearly reconstructed by the hybridization with the vacancy. This reconstruction behavior is clearly observed when the structural effect is suppressed through Brewster geometry in RSXS measurement, leading to the additional anisotropic effect in the doped BCFO. Eventually, electrons hopping behavior around the Fermi level is disturbed by the additional anisotropic effect that attributes to the localized orbital bands, reinforcing insulating behavior on the BCFO.

In summary, we have experimentally demonstrated the role of oxygen vacancy which is confined into the two-dimensional self-assembled layers occurring periodically at a few nanometers interval in the Ca-doped $BiFeO_3$ films by using XAS and RSXS techniques. The central finding here is that the orbital state of Fe^{3+} cation is modified via the hybridization with the oxygen vacancy, which is competing with the electronic configuration of the Fe valence band in BCFO. This gives a key idea why with increasing

doping ratio the diode effect of BiFeO₃ becomes weak even in higher contents of the oxygen vacancy in the previous report²². These microscopic aspects of oxygen vacancies open a window into a new regime of energy materials, and oxides in general.

Methods

Sample preparation. Using pulsed laser deposition (KrF excimer laser, $\lambda = 248$ nm), BCFO films were grown on SrTiO₃ (001) substrates at 600–700 °C in 50–100 mTorr oxygen pressure. The films were cooled down at a rate of 5 °C/min with an oxygen pressure of ~ 1 atm. With increasing the x ratio, practically the oxygen vacancy in BCFO film is increasing^{15,18}. As varying Ca substitution ratio ($x = 0.075 \sim 0.30$), we monitored BCFO films' superstructural form, including crystalline quality, using by X-ray diffraction with Cu $K_{\alpha 1}$ ($\lambda = 1.54$ Å) radiation (see Fig. 1b). Aiming to manipulate the periodicity of the oxygen vacancy which is confined around interfaces of the superstructure, finally, the x range was chosen to 0.20, 0.25, and 0.30 (see Supplementary Information).

Synchrotron experiments. The XAS spectra show white line resonances at the Fe $L_{2,3}$ -edges. The spectra result from Fe $2p \rightarrow 3d$ dipole transitions, are divided roughly into the L_3 ($2p_{3/2}$) and L_2 ($2p_{1/2}$) regions. For the LD measurements via XAS, the polarization direction of the linearly polarized X-rays (98% polarized) was tuned by elliptically polarized undulator, with horizontal (σ) and vertical (π) polarizations corresponding to complete in-plane ($E//a$) and majority out-of-plane ($E//c$) polarized components,

respectively (see Fig. 2b). These spectroscopic experiments, XAS and RSXS, were carried out at beamlines 8-2 and 13-3 of the Stanford Synchrotron Radiation Lightsource (SSRL). Note that all measurements were done by zero-electric field polarization.

Atomic multiplet calculations. The calculations were carried out for the configuration interaction via combination between the initial $2p^63d^5$ state and its charge transfer $2p^63d^6\bar{L}$ state under the D_{4h} crystal symmetry. The used Coulomb interactions are $U_{dd} = 5$ eV and $U_{pd} = 6$ eV. The charge transfer energy is $\Delta = 2.7$ eV. The crystal field ($10D_q = 1.6$ eV) was used for this calculation. The Slater integrals are with $\sim 80\%$ of the atomic values.

References

1. Muller, D. A., Nakagawa, N., Ohtomo, A., Grazul, J. L. & Hwang, H. Y. Atomic-scale imaging of nanoengineered oxygen vacancy profiles in SrTiO₃. *Nature* **430**, 657–661 (2004).
2. Alloul, H., Bobroff, J., Gabay, M. & Hirschfeld, P. J. Defects in correlated metals and superconductors. *Rev. Mod. Phys.* **81**, 45–108 (2009).
3. Pavlenko, N., Kopp, T., Tsymbal, E. Y., Sawatzky, G. A. & Mannhart, J. Magnetic and superconducting phases at the LaAlO₃/SrTiO₃ interface: The role of interfacial Ti 3d electrons *Phys. Rev. B* **85**, 020407 (2012).
4. Lee, H. S., Choi, S. G., Park, H.-H. & Rozenberg, M. J. A new route to the Mott-Hubbard metal-insulator transition: Strong correlations effects in Pr_{0.7}Ca_{0.3}MnO₃. *Sci. Rep.* **3**, 1704 (2013).
5. Bhattacharya, A. & May, S. J. Magnetic Oxide Heterostructures. *Annu. Rev. Mater. Res.* **44**, 65–90 (2014).
6. Song, J. *et al.* Role of Oxygen Vacancies on the Performance of Li[Ni_{0.5-x}Mn_{1.5+x}]O₄ ($x = 0, 0.05, \text{ and } 0.08$) Spinel Cathodes for Lithium-Ion Batteries. *Chem. Mater.* **24**, 3101–3109 (2012).
7. Muñoz-García, A. B. *et al.* Unveiling Structure–Property Relationships in Sr₂Fe_{1.5}Mo_{0.5}O_{6- δ} , an Electrode Material for Symmetric Solid Oxide Fuel Cells. *J. Am. Chem. Soc.* **134**, 6826–6833 (2012).
8. Sushko, P. V., Rosso, K. M., Zhang, J.-G., Liu, J. & Sushko, M. L. Li-Ion Batteries: Oxygen Vacancies and Ordering of *d*-levels Control Voltage Suppression in Oxide Cathodes: the Case of Spinel LiNi_{0.5}Mn_{1.5}O_{4- δ} . *Adv. Funct. Mater.* **23**, 5454–5454

- (2013).
9. Varley, J. B., Viswanathan, V., Nørskov, J. K. & Luntz, A. C. Lithium and oxygen vacancies and their role in Li_2O_2 charge transport in $\text{Li}-\text{O}_2$ batteries. *Energy Environ. Sci.* **7**, 720–727 (2014).
 10. Choi, T., Lee, S., Choi, Y. J., Kiryukhin, V. & Cheong, S.-W. Switchable Ferroelectric Diode and Photovoltaic Effect in BiFeO_3 . *Science* **324**, 63–66 (2009).
 11. Yi, H. T., Choi, T., Choi, S. G., Oh, Y. S. & Cheong, S.-W. Mechanism of the Switchable Photovoltaic Effect in Ferroelectric BiFeO_3 . *Adv. Mater.* **23**, 3403–3407 (2011).
 12. Moubah, R. *et al.* Photoelectric Effects in Single Domain BiFeO_3 Crystals. *Adv. Funct. Mater.* **22**, 4814–4818 (2012).
 13. Guo, Y., Guo, B., Dong, W., Li, H. & Liu, H. Evidence for oxygen vacancy or ferroelectric polarization induced switchable diode and photovoltaic effects in BiFeO_3 based thin films. *Nanotechnology* **24**, 275201 (2013).
 14. Gao, R. L. *et al.* Oxygen vacancies induced switchable and nonswitchable photovoltaic effects in $\text{Ag}/\text{Bi}_{0.9}\text{La}_{0.1}\text{FeO}_3/\text{La}_{0.7}\text{Sr}_{0.3}\text{MnO}_3$ sandwiched capacitors *Appl. Phys. Lett.* **104**, 031906 (2014).
 15. Yang, C.-H. *et al.* Electric modulation of conduction in multiferroic Ca-doped BiFeO_3 films. *Nat. Mater.* **8**, 485–493 (2009).
 16. Bharathi, *et al.* Detection of electrically formed photosensitive area in Ca-doped BiFeO_3 thin films. *Appl. Phys. Lett.* **102**, 012908 (2013).
 17. Würfel, P. *Physics of solar cells: from basic principles to advanced concepts; Physics textbook*, 2nd, updated and expanded ed., Wiley-VCH: Weinheim (2009).

18. Yamamura, H. & Kiriyama, R. The Relations between Oxygen Vacancies and Structures in the Solid Solution Systems $\text{Sr}_{1-x}\text{M}_x\text{FeO}_{3-\delta}$ (M=Y, La, Bi and In). *Nippon Kagaku Kaishi* **1972**, 343–349 (1972).
19. Schiemer, J. *et al.* Detailed Phase Analysis and Crystal Structure Investigation of a $\text{Bi}_{1-x}\text{Ca}_x\text{FeO}_{3-x/2}$ Perovskite-Related Solid Solution Phase and Selected Property Measurements Thereof. *Chem. Mater.* **21**, 4223–4232 (2009).
20. Rossell, M., Ramasse, Q., Erni, R., Yang, C.-H. & Ramesh, R. Atomic Configuration of Planar Defects in Multiferroic Ca-doped BiFeO_3 Films. *Microsc. Microanal.* **16**, 96–97 (2010).
21. Withers, R. L., Schiemer, J., Bourgeois, L., Norén, L. & Liu, Y. A careful phase analysis and TEM investigation of the incommensurately modulated, $(\text{Bi}_{1-x}\text{M}^{\text{II}})\text{Fe}^{\text{III}}\text{O}_{3-x/2}$ (M = Ca and Sr), solid solution phases. *J. Phys. Conf. Ser.* **226**, 012015 (2010).
22. Tu, C. S. *et al.* Calcium-doping effects on photovoltaic response and structure in multiferroic BiFeO_3 ceramics. *J. Appl. Phys.* **114**, 124105 (2013).
23. Abbate, M. *et al.* Controlled-valence properties of $\text{La}_{1-x}\text{Sr}_x\text{FeO}_3$ and $\text{La}_{1-x}\text{Sr}_x\text{MnO}_3$ studied by soft-x-ray absorption spectroscopy. *Phys. Rev. B* **46**, 4511–4519 (1992).
24. Kim, J.-Y., Koo, T. Y. & Park, J.-H. Orbital and Bonding Anisotropy in a Half-Filled GaFeO_3 Magnetoelectric Ferrimagnet. *Phys. Rev. Lett.* **96**, 047205 (2006).
25. Yu, P. *et al.* Interface Ferromagnetism and Orbital Reconstruction in BiFeO_3 – $\text{La}_{0.7}\text{Sr}_{0.3}\text{MnO}_3$ Heterostructures. *Phys. Rev. Lett.* **105**, 027201 (2010).
26. Staub, U. Advanced resonant soft x-ray diffraction to study ordering phenomena in magnetic materials. *J. Phys. Conf. Ser.* **211**, 012003 (2010).

27. Tanaka, A. *et al.* Symmetry of Orbital Order in Fe₃O₄ Studied by Fe L_{2,3} Resonant X-Ray Diffraction. *Phys. Rev. Lett.* **108**, 227203 (2012).
28. De Groot, F. M. F., Fuggle, J. C., Thole, B. T. & Sawatzky, G. A. 2p x-ray absorption of 3d transition-metal compounds: An atomic multiplet description including the crystal field. *Phys. Rev. B* **42**, 5459–5468 (1990).
29. Ikeno, H., de Groot, F. M. F., Stavitski, E. & Tanaka, I. Multiplet calculations of L_{2,3} x-ray absorption near-edge structures for 3d transition-metal compounds. *J. Phys. Condens. Matter* **21**, 104208 (2009).
30. Cao, G. L. *et al.* Oxygen-vacancy ordering in multiferroic Bi_{1-x}Ca_xFeO_{3-x/2} (0.1 ≤ x ≤ 0.5). *Europhys. Lett.* **102**, 27002 (2013).
31. Brewster, D. On the laws which regulate the polarisation of light by reflexion from transparent bodies. *Philos. Trans. R. Soc. Lond.* **105**, 125–159 (1815).
32. Hill, J. P. & McMorrow, D. F. Resonant Exchange Scattering: Polarization Dependence and Correlation Function. *Acta Crystallogr. A* **52**, 236–244 (1996).

Acknowledgements

We thank Dr. Kevin Hunter Stone for useful discussions. Synchrotron studies were carried out at the SSRL, a Directorate of SLAC and an Office of Science User Facility operated for the US DOE Office of Science by Stanford University. J.L. acknowledges support by the Department of Energy, Office of Basic Energy Sciences, Materials Sciences and Engineering Division, under contract DE-AC02-76SF00515. This work at KAIST was supported by the National Research Foundation (NRF) Grant funded by the Korean Government (NRF-2013S1A2A2035418, 2014R1A2A2A01005979).

Author contributions statement

H.J., C.Y., and J.-S.L. planned the experiments. H.J., G.K., and J.-S.L. carried out the Fe *L*-edge and O *K*-edge soft x-ray diffraction experiments at SSRL. H.J., C.Y., C.K., and J.-S.L. contributed to the data interpretation and modeling discussions. J.L. and C.Y. grew the samples. H.J. and J.-S.L. wrote the manuscript with contributions from the other authors. J.-S.L. is responsible for overall project direction, planning, and management.

Additional information

Competing financial interests: The authors declare no competing financial interests.

Figures

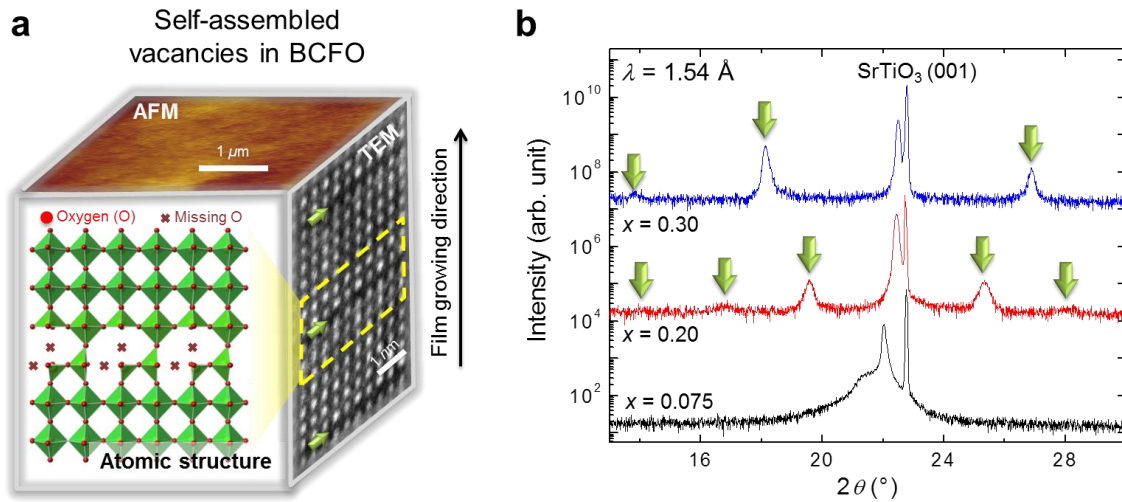


Figure 1. (a) Conceptual atomic structure shows a schematic picture of the self-assembled vacancies in the doped BCFO. AFM reveals the flatness of the film surface. TEM image, taken from our previous work²⁰ [Copyright notice. Reprinted with the permission], indicates the location oxygen vacancy with respect to the growing direction. The green arrows indicate the vacancy position. (b) Confirmation of the superstructural formation of oxygen vacancy in BCFO films using X-ray diffraction. The films ($x \geq 0.2$) show clear superstructure (indicated by green arrows) reflections. Central sharp peak corresponds to substrate SrTiO_3 (001) and adjacent lower angle peaks indicate BCFO film.

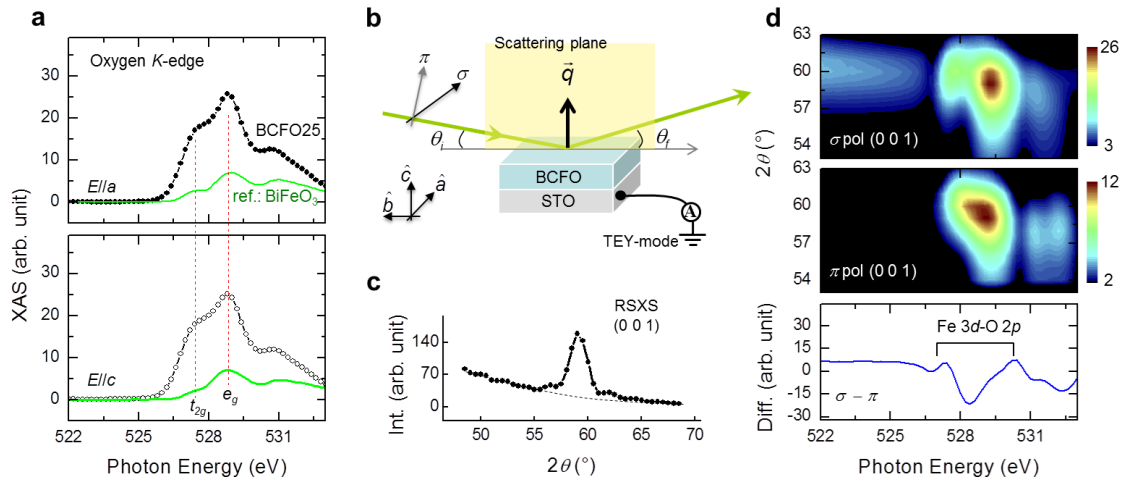


Figure 2. (a) O K -edge XAS spectra of BCFO25 with $E // a$ and $E // c$. The spectra are compared to the scaled reference (bulk BiFeO₃) spectra. Dashed red lines denote energy positions of t_{2g} and e_g orbital states (b) Experimental configuration for XAS and RSXS experiments. θ_i and θ_f denote incident and scattered angles, respectively. For XAS experiment, θ_i was set by 20° – $E // a$ ($E // c$) was measured in σ (π) polarization. (c) Superstructure reflection of BCFO25, $\mathbf{q} = (001)$ at 525 eV. Dashed line is estimated by the specular background. (d) O K -edge RSXS profiles of (001) reflection using σ and π polarization, and the polarization difference of angle integrated energy profiles.

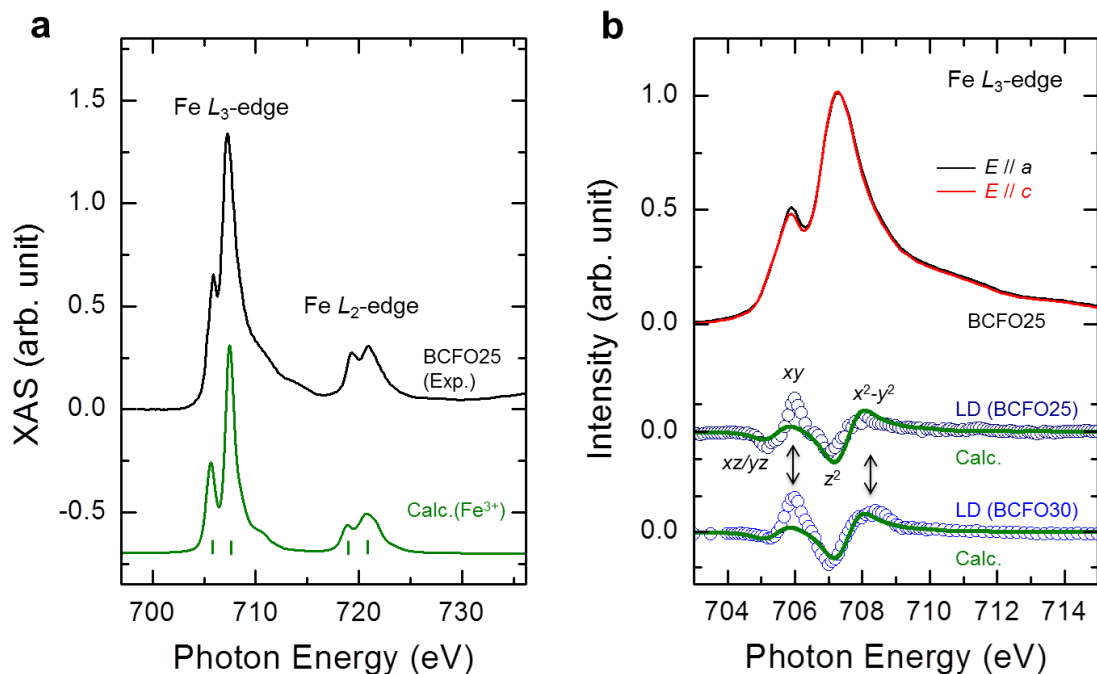


Figure 3. (a) XAS spectrum at Fe $L_{2,3}$ -edges on BCFO25. The spectrum is compared to a calculated spectrum of Fe^{3+} in D_{4h} symmetry. In the calculation, the vertical bars denote the atomic states. (b) Polarization dependence of BCFO25 with $E // a$ and $E // c$. LD spectra of BCFO25 and BCFO30, which are compared with calculated LD of Fe^{3+} in D_{4h} symmetry. Arrows indicate a discrepancy between experiments and calculation.

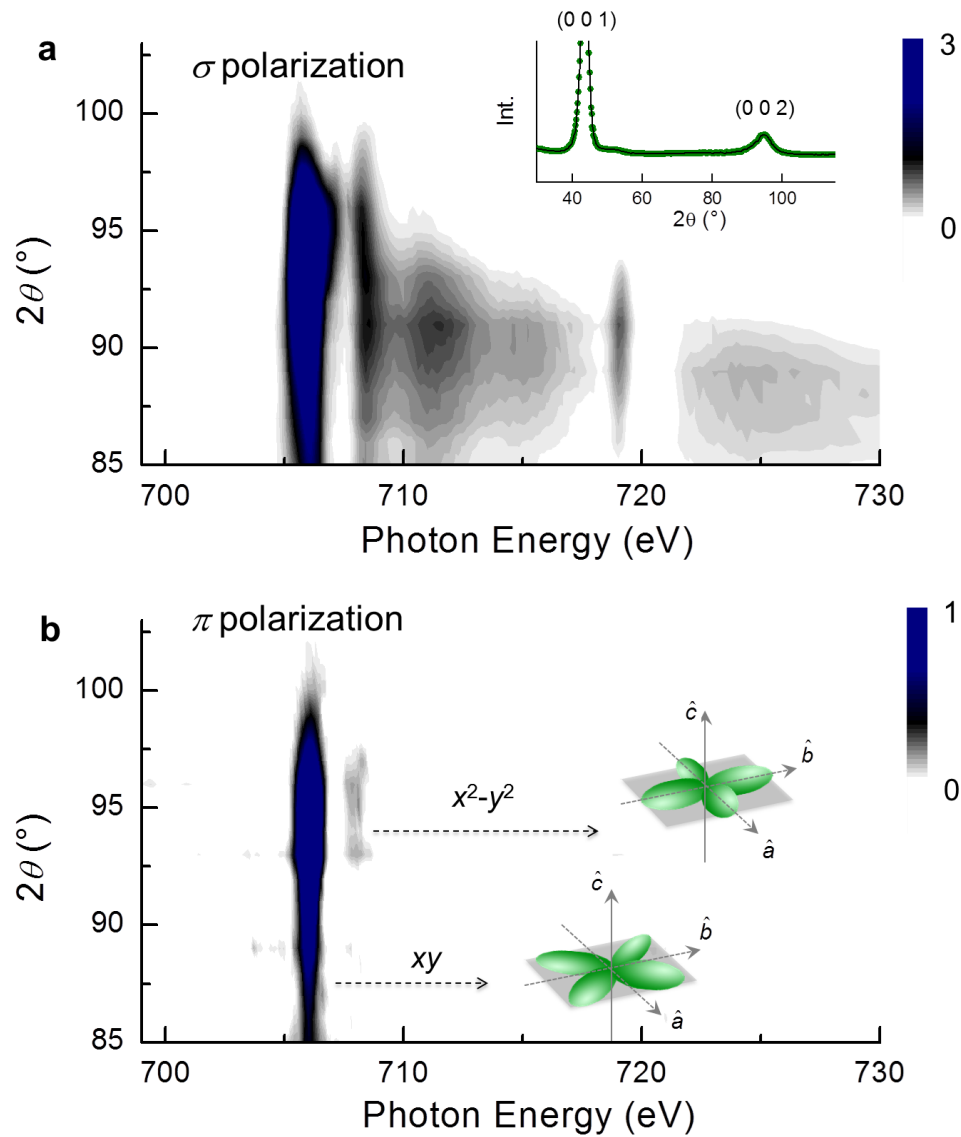


Figure 4. Fe $L_{2,3}$ -edge RSXS profiles. All profiles are corrected by fluorescence background. (a) The profile at $q = (002)$ was taken by incident σ polarization. Inset shows full θ - 2θ scan. (b) The profile at $q = (002)$ was taken by incident π polarization. Two pronounced features at $E = 706$ eV and 708 eV are corresponding to in-plane xy and x^2-y^2 orbital states. Arrows indicate cartoon illustrations of those orbitals

Supplementary Information for

Orbital Reconstruction in a Self-assembled Oxygen Vacancy Nanostructure

H. Jang¹, G. Kerr¹, J. S. Lim², C.-H. Yang², C.-C. Kao³, and J.-S. Lee^{1,}*

*¹Stanford Synchrotron Radiation Lightsource, SLAC National Accelerator Laboratory,
Menlo Park, California 94025, USA*

²Department of Physics, KAIST, Yuseong-gu, Daejeon 305-701, South Korea

³SLAC National Accelerator Laboratory, Menlo Park, California 94025, USA

**jslee@slac.stanford.edu*

[S. 1] Manipulation of a periodicity of oxygen vacancy

When Ca^{2+} substitution rate (x) is larger than ~ 0.15 , oxygen vacancy superstructure is formed^{S1} and the periodicity empirically shows $\sim 1.5/x$. When x becomes 0.20, 0.25, and 0.30, the periodicity becomes 8 unit cells (u.c.), 6 u.c., and 5 u.c., respectively and corresponding superstructure reflection positions changed (Fig. S1). When $x = 0.25$, 2θ angle of second superstructure reflection (002) is near 90° and therefore the structural contributions are suppressed with π polarized incident light (see section [S. 2] for details).

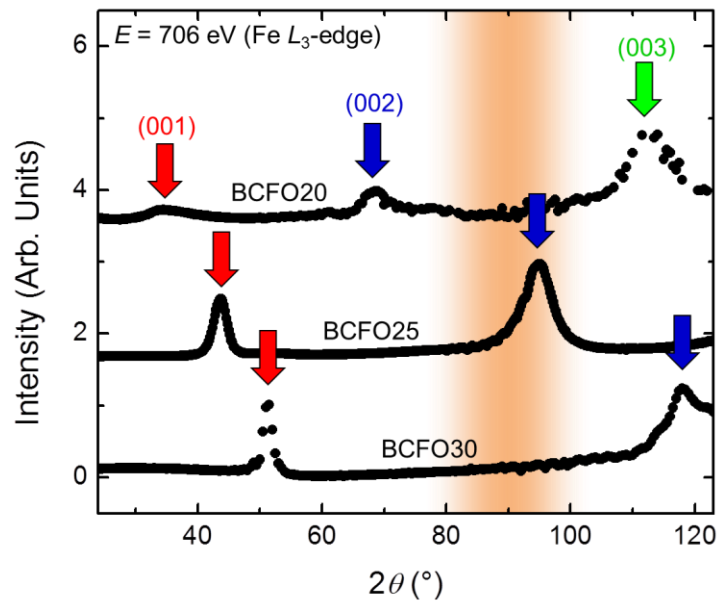


Figure S1. Manipulating the periodicity of the oxygen vacancy ordering by Ca^{2+} substitution ratio. First, second, and third superstructure reflections are indicated by red, blue, and green colored arrows, respectively. The intensities are divided by Q^4 and shifted for clarity, where Q is the absolute value of momentum transfer in unit of \AA^{-1} . Orange area near $2\theta = 90^\circ$ indicates the vicinity of Brewster's angle.

[S. 2] Brewster's angle and suppression of structural signal at $2\theta = 90^\circ$ and selection of (002) reflection of BCFO25

When a light strikes a surface, the amount of reflection and transmission is determined by refractive index of the target material (n), incident angle (θ_i), and polarization rate of the light. Geometry of incident and scattered light is shown in Fig. S2a. At a certain incident angle, no π polarized light is reflected. The angle is called as Brewster's angle ($\theta_B = 90^\circ - \theta_i$) and determined by $\tan \theta_B = n/n_0$, where n_0 is a refractive index of vacuum^{S2}. In x-ray region, n is very close to 1, and therefore θ_B is nearly identical to 45° (Fig. S2b).

In general, intensity of Thomson scattering which is from structural contribution is determined by $(\varepsilon_i \cdot \varepsilon_f)$ where ε_i (ε_f) is polarization of incident (scattered) light^{S3}. Since we only control a polarization of the incident x-ray polarization, the scattered photon's polarization always shows both σ_f and π_f polarizations. In this sense, when we use the π as the ε_i , the term, $\pi_i \cdot \sigma_f$, becomes zero. This is because an angle between two polarizations' directions is orthogonal. Therefore, the structural contribution is determined solely by $\pi_i \cdot \pi_f$ in the π channel. When $2\theta = \theta_i + \theta_f = 90^\circ$ (Fig. S2b), $\pi_i \cdot \pi_f$ also becomes zero. Consequently, with π polarized light, there is little structural contribution from either reflection or diffraction near $2\theta = 90^\circ$ (e.g. BCFO25 (002) reflection as shown in Fig. S1). Furthermore, we need to consider an addition polarization term in the resonant x-ray scattering, i.e., $(\varepsilon_i \times \varepsilon_f)$ ^{S3}, showing the 2×2 polarization matrix. Diagonal terms in the matrix are proportional to isotropic form factor (i.e., structural factor), which is similar effect in $(\varepsilon_i \cdot \varepsilon_f)$. Off-diagonal terms in the matrix are

sensitive to detect anisotropic contributions such as spin, orbital, and charge disproportion.

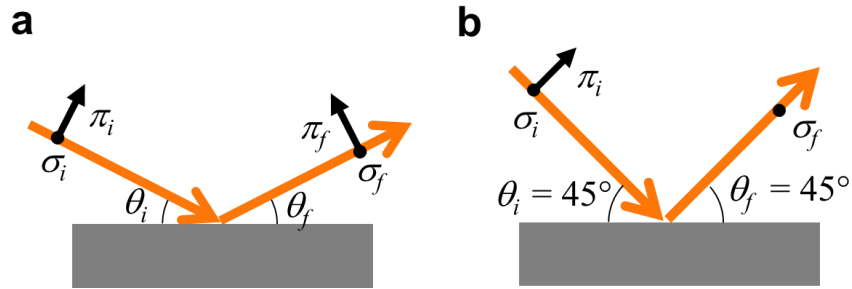


Figure S2. (a) Simple description of incident and scattered x-ray geometry with incident (θ_i) and scattered angle (θ_f) with linear polarization (σ, π). (b) At Brewster's angle position ($\theta_i = \theta_f = 45^\circ$), no structural contribution from π polarized light.

[S. 3] Subtraction of diffuse scattering

Even in diffraction condition, unexpected signals can be detected as well as pure diffraction signal. One of them is fluorescence background. It is photon energy dependent but there is little angle dependence. Therefore, if we subtract a signal from out of diffraction condition, we can remove fluorescence background.

Fig. S3a shows rocking (θ) scan of BCFO25 (002) reflection. Figure S3b and S3c show RSXS profiles at both on diffraction condition (red colored arrow in Fig. S3a) and diffuse condition conditions (blue colored arrow in Fig. S3a) of (002) in incident σ

polarization and π polarization, respectively. σ_i RSXS profile contains complicated structural modification by oxygen vacancy (Fig. S3b). In π_i , structural contribution is suppressed, and therefore nearly pure electronic signal can be obtained (Fig. 4b in main article). (001) reflection which is away from Brewster's angle show complicated structural contribution in both σ_i and π_i cases (Fig. S4).

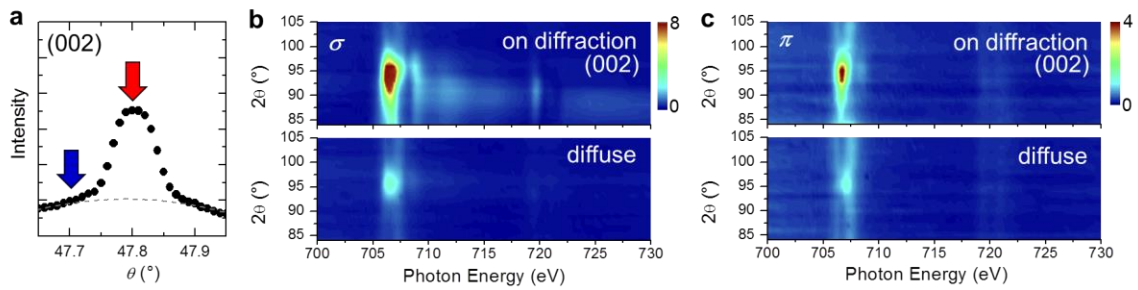


Figure S3. (a) Red and blue colored arrow indicate the position of on diffraction and diffuse conditions of (002) reflection. RSXS profiles on diffraction condition and diffuse condition of (b) (002) with σ_i and (c) (002) with π_i .

Complicated structural contribution is suppressed with π_i in contrast to structural contribution dominant σ_i case.

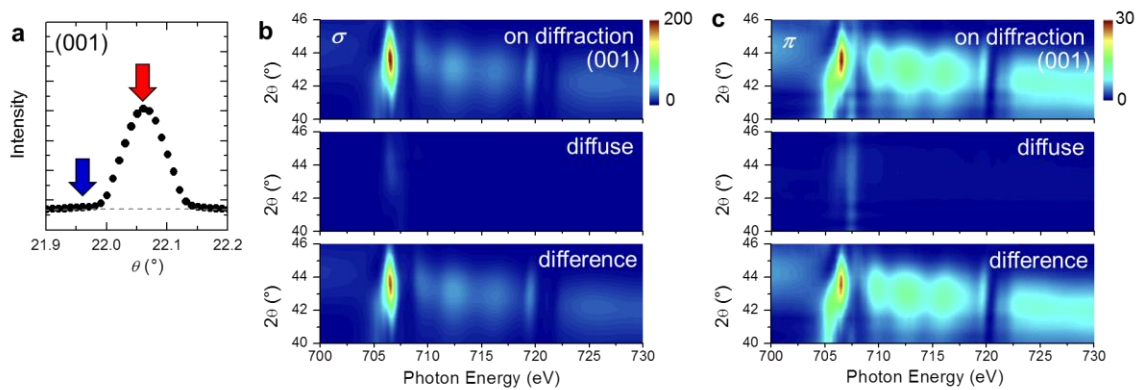


Figure S4. (a) Red and blue colored arrow indicate the position of on diffraction and diffuse conditions of (001) reflection. RSXS profiles at on diffraction condition, diffuse condition, and their difference of (b) (001) with σ_i and (c) (001) with π_i

REFERENCES

- S1. Yang, C.-H. *et al.* Electric modulation of conduction in multiferroic Ca-doped BiFeO₃ films. *Nat. Mater.* **8**, 485–493 (2009).
- S2. Brewster, D. On the laws which regulate the polarisation of light by reflexion from transparent bodies. *Philos. Trans. R. Soc. Lond.* **105**, 125–159 (1815).
- S3. Hill, J. P. & McMorrow, D. F. Resonant Exchange Scattering: Polarization Dependence and Correlation Function. *Acta Crystallogr. A* **52**, 236–244 (1996).